Monthly Notices of the ROYAL ASTRONOMICAL SOCIETY

MNRAS **469,** 4268–4282 (2017) doi:10.1093/mnras/stx1140
Advance Access publication 2017 May 11

High-cadence spectroscopy of M-dwarfs – II. Searching for stellar pulsations with HARPS

Z. M. Berdiñas,[1]★ C. Rodríguez-López,[1] P. J. Amado,[1] G. Anglada-Escudé,[2] J. R. Barnes,[3] J. MacDonald,[4] M. Zechmeister[5] and L. F. Sarmiento[5]

[1]*Instituto de Astrofísica de Andalucía – CSIC, Glorieta de la Astonomía s/n, E-18008 Granada, Spain*
[2]*School of Physics and Astronomy, Queen Mary University of London, 327 Mile End Rd., London E1 4NS, UK*
[3]*Department of Physical Sciences, The Open University, Walton Hall, Milton Keynes MK7 6AA, UK*
[4]*Department of Physics and Astronomy, University of Delaware, Newark, DE 19716, USA*
[5]*Institut für Astrophysik, Georg-August-Universität Göttingen, Friedrich-Hund-Platz 1, D-37077 Göttingen, Germany*

Accepted 2017 May 9. Received 2017 May 8; in original form 2016 August 1

ABSTRACT

Stellar oscillations appear all across the Hertzsprung–Russell diagram. Recent theoretical studies support their existence also in the atmosphere of M dwarfs. These studies predict for them short periodicities ranging from 20 min to 3 h. Our Cool Tiny Beats (CTB) programme aims at finding these oscillations for the very first time. With this goal, CTB explores the short time domain of M dwarfs using radial velocity data from the High Accuracy Radial velocity Planet Searcher (HARPS)-European Southern Observatory and HARPS-N high-precision spectrographs. Here we present the results for the two most long-term stable targets observed to date with CTB, GJ 588 and GJ 699 (i.e. Barnard's star). In the first part of this work we detail the correction of several instrumental effects. These corrections are especially relevant when searching for subnight signals. Results show no significant signals in the range where M dwarfs pulsations were predicted. However, we estimate that stellar pulsations with amplitudes larger than $\sim$0.5 m s^{-1} can be detected with a 90 per cent completeness with our observations. This result, along with the excess of power regions detected in the periodograms, opens the possibility of non-resolved very low amplitude pulsation signals. Next generation more precise instrumentation would be required to detect such oscillations. However, the possibility of detecting pulsating M-dwarf stars with larger amplitudes is feasible due to the short size of the analysed sample. This motivates the need for completeness of the CTB survey.

Key words: techniques: radial velocities – stars: individual: GJ 588 – stars: individual: GJ 699 – stars: low-mass – stars: oscillations.

1 INTRODUCTION

Our Galaxy is mostly populated by low-mass stars. In particular, more than 72 per cent of our stellar neighbours are main-sequence stars with masses ranging from 0.08 up to 0.60 M$_\odot$ (Henry et al. 2006). A better modelling of the fundamental physical properties of these abundant low-mass stars is important, not just to better understand the stars themselves, but also to address fundamental questions such as their contribution to the total mass of our Galaxy; a parameter with cosmological implications that still requires a precise derivation of the mass–luminosity relation for different metallicities.

The theory of asteroseismology, which studies the seismology of the stars, has been demonstrated to be a powerful tool to refine the models that describe the stellar structure and evolution (i.e. the combination of seismic data with classical astronomical observations makes possible to calibrate the theoretical models). Additionally, using the asteroseismology we can infer the properties of the stellar interiors. This allows us to calculate at an unprecedented level of accuracy not only the main physical parameters of the star, but also of its hosted planets. Consequently, parameters such as the planet mass, radius or even the average surface temperature or the planet orbit obliquity can be measured at a very high precision level (e.g. Kepler-10, Kepler-56 or Kepler-419; Huber et al. 2013; Dawson et al. 2014; Fogtmann-Schulz et al. 2014).

Recently, a new theoretical study from Rodríguez-López et al. (2014, hereafter RL14) predicts that low-mass M-dwarf stars

★ E-mail: zaira.modrono.berdinas@gmail.com

(0.3–0.6 $M_{\odot}$) have the potential to pulsate. Consequently, M dwarfs may have mechanisms able to start, drive and maintain stellar pulsations in their interior. This opens the possibility for the application of asteroseismic tools to M dwarfs, but first the pulsations have to be observationally confirmed.

RL14 predict two main regions where M dwarfs may be able of maintaining pulsations. While one comprises young pre-main-sequence stars, the other is formed by M dwarfs on the main sequence. For the latter, which corresponds to the M dwarfs observed with our observational programme, RL14 predict pulsation periods in the 20 min up to 3 h range (8–72 d^{-1} in frequency). Two driving mechanisms are at work to maintain the oscillations: (i) the ϵ mechanism, caused by He^3 burning, that works on its own in the 20–30 min range for completely convective models (0.20–0.30 $M_{\odot}$) and (ii) the so-called 'flux-blocking mechanism' that acts periodically blocking the radiative flux at the tachocline (i.e. the transition layer from the radiative interior and the convective exterior), and that is the main driver of the pulsations in the whole 20 min to 3 h range for models with masses in the 0.35–0.60 $M_{\odot}$ range. RL14 is an extension of Rodríguez-López, MacDonald & Moya (2012) to include the excitation of not just the fundamental radial mode, but also non-radial and non-fundamental p modes and g modes. Such a range of predicted periods gives us a starting point to start the search for stellar pulsations in main-sequence stars.

Even though the theory works well in predicting the expected periods, the current existing linear oscillation codes cannot predict the amplitudes of the oscillations. So far, photometric campaigns have only been able to establish upper limits on the amplitudes. Indeed, Rodríguez et al. (2016) have recently performed an extensive and exhaustive analysis of 87 M dwarfs observed at highprecision and short cadence (1 min) with the *Kepler* spacecraft. Although they did not find any significant signal in the 10–100 d^{-1} range, they set up a new photometric detection threshold of tens of μmag. However, this low photometric limit does not imply that stellar pulsations are undetectable using high-precision radial velocity (RV) spectrographs. In fact, radial and non-radial pulsation modes detected in both, photometric and spectroscopic observations for other spectral types, indicate that a signal of 10 μmag can have a counterpart of 1 m s^{-1} in RVs (e.g. δ Scuti and γ Dor oscillators such as FG Vir, RZ Cas, 9-Aur, HR 8799, gam Dor and HD 49434; Krisciunas et al. 1995; Zerbi et al. 1997, 1999; Lehmann & Mkrtichian 2004; Zima et al. 2006; Uytterhoeven et al. 2008); an amplitude that is detectable with High Accuracy Radial velocity Planet Searcher (HARPS)-European Southern Observatory (ESO), which has a reported RV precision in the short term of 0.5 m s^{-1} (Lovis & Fischer 2010).

Motivated by this favourable relation we started in 2013 the Cool Tiny Beats (CTB) project, which uses the high-precision RV spectrographs HARPS-ESO (hereafter HARPS) and HARPS-N with the goal of detecting stellar pulsations in M dwarfs for the first time. We present the first results of the CTB programme on the search for stellar pulsations. In particular, we present the analysis on the most long-term-stable stars of our sample observed up to date with CTB; GJ 588 and GJ 699 (also known as Barnard's star). This paper is organized as follows. Section 2 introduces the CTB survey, observations and data reduction. In Section 3 we discuss and correct the data from instrumental effects. Section 4 is the main part of this study comprising the search for periodic signals embedded in the GJ 588 and GJ 699 time series (Subsection 4.1), a short discussion about the pulsation modes we could expect on GJ 588 (Subsection 4.2) and the empirical calculation of HARPS precision limit in the high-cadence domain (Subsection 4.3). Finally, in Section 5 we give the main conclusions of this work.

2 THE CTB PROGRAMME: OBSERVATIONS AND DATA REDUCTION

In addition to the high-precision spectroscopy, a continuous time monitoring of the target is essential in asteroseismic campaigns. With CTB we have been exploring the short-time domain of a sample of bright M dwarfs with the scientific objective of confirming the predicted, but still undetected, stellar pulsations of M dwarfs. In particular, we performed high-cadence observations, meaning in this case that we continuously monitored the same target with exposures shorter than 20 min during several consecutive nights. This observational strategy assists also in the robust detection of small planets in warm/potentially habitable orbits around the stars, other of the CTB science goals (e.g. Anglada-Escudé et al. 2016a). In addition to that, understanding the Doppler variability of the targets is very valuable (even necessary) in the interpretation of the noise sources that can potentially inject false positives in periods of a few days to weeks (Anglada-Escudé et al. 2016b). Compared to the classical planet searches, the unusual high-cadence sampled by CTB allowed us to explore the behaviour of the instrument within the night, identify sources of systematic noise and correct for them in some cases (e.g. Berdiñas et al. 2016).

The CTB initial sample was comprised of 25 M dwarfs. The targets were mostly selected to lie within the boundaries of one of the instability regions defined in RL14, in particular, the one mainly comprised of main-sequence M stars. Other criteria were to have demonstrate long-term Doppler stability (Δ_v(rms) < 2.5 m s^{-1}), low activity levels and slow rotation. Such a sample would satisfy the requirements for both the asteroseismology and planetary science cases of CTB. In Fig. 1 we show the initial CTB sample on a $T_{\rm eff}$–log g diagram. We have highlighted GJ 588 and GJ 699 (Banard's star), focus of this study, with a black square and a red dot, respectively. For a future CTB Phase II programme we plan to update our sample including more targets on both instability regions predicted by RL14.

Barnard's star is an extensively studied M dwarf that does not have any reported planets and it is known to be stable in the long term (e.g. Zechmeister, Kürster & Endl 2009 derived a RV stability of 2.70 m s^{-1} after subtracting the secular acceleration[1] using Ultraviolet and Visual Echelle Spectrograph (UVES) data, later Anglada-Escudé & Butler 2012 reduced the limit down to 1.23 m s^{-1} using HARPS, and more recently, Choi et al. 2013 found no significant periodic Doppler signals with amplitudes above ∼2 m s^{-1} using 25 yr of data from the Lick and Keck Observatories). In fact CTB uses GJ 699 as its RV standard. That is, in addition to the high-cadence observations presented here, we usually took at least one spectrum of GJ 699 per night when it was observable. For this reason, even when GJ 699 lies in the outer edge of the theoretical instability region, we decided to include it in this study – the instability region gives us a starting point in the search for pulsations, but we should not necessarily exclude targets close to its edge since its boundaries were not yet observationally constrained. On the other hand, GJ 588 is both stable and lies well within the predicted instability region. We show the relevant stellar parameters of GJ 588 and GJ 699 in Table 1.

The asteroseismology case of CTB requires of high-precision spectroscopy. This is the reason why the programme makes use of HARPS and HARPS-N, the most stable current instrumentation

[1] The secular acceleration effect is caused by the high proper motion of the nearby stars and results in a linear trend in the RVs.

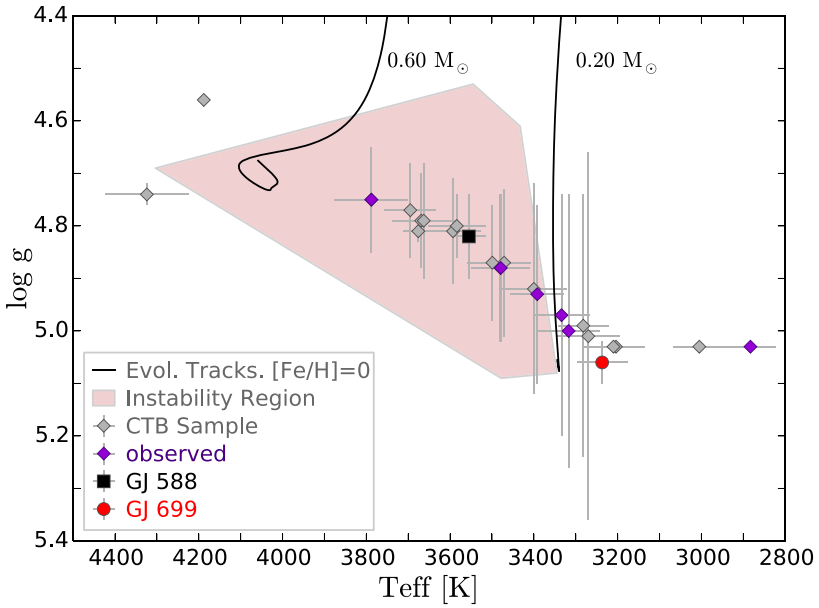

Figure 1. Instability region (pink area) of main-sequence M dwarfs predicted by RL14. The black square and red dot correspond to GJ 588 and GJ 699, respectively. The diamonds indicate other CTB targets, where in purple we highlight those that have been already observed. The black solid lines are 0.20 and 0.60 $M_{\odot}$ evolutionary tracks (solar metallicity and mixing length parameter $\alpha = 1$) delimiting the instability region. Physical parameters come from: Gaidos et al. (2014), Boyajian et al. (2012), Santos et al. (2013), Dressing & Charbonneau (2013) and Steffen & Farr (2013).

Table 1. GJ 588 and GJ699 stellar parameters.

Parameters	GJ 588	GJ 699	Refs
SpT	M2.5	M4	RE95
V_{mag}	9.31	9.51	KO10
Dist. (pc)	5.93 ± 0.05	1.82 ± 0.01	KO10
P_{rot} (d) [a]	61.3 ± 6.5	148.6 ± 0.1	SU15
$v \sin i$ (km s^{-1})	<3.0	<2.5	RE12
[Fe/H] (dex)	0.06 ± 0.08	-0.51 ± 0.09	NE14
T_{eff} (K)	3555 ± 41	3237 ± 60	GA14
M ($M_{\odot}$)	0.43 ± 0.05	0.15 ± 0.02	GA14, BO12
R ($R_{\odot}$)	0.42 ± 0.03	0.187 ± 0.001	GA14, BO12
log g (cm s^{-2}) [b]	4.82 ± 0.08	5.040 ± 0.005	

Notes. References: BO12 – Boyajian et al. (2012); GA14 – Gaidos et al. (2014); KO10 – Koen et al. (2010); NE14 – Neves et al. (2014); RE95 – Reid, Hawley & Gizis (1995); RE12 – Reiners, Joshi & Goldman (2012); SU15 – Suárez Mascareño et al. (2015).
[a]SU15 also used CTB data to calculate the P_{rot} values.
[b]The log g values were obtained from this table parameters.

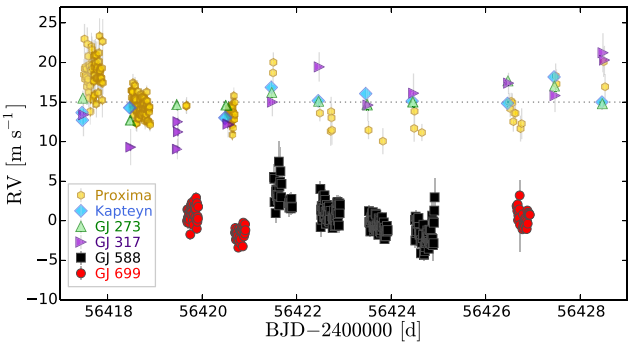

Figure 2. RVs of the CTB 2013 May run from HARPS. Six targets were observed during 11 nights. GJ 588 (black squares) and GJ 699 (red dots) are the focus of this study. The RVs of the other targets (Proxima Centauri, yellow hexagons; Kapteyn's star, blue diamonds; GJ 273 or Luyten's star, green up triangles; and GJ 317, purple right triangles) were shifted +15 m s^{-1} for visualization reasons.

of this kind. In particular, the data presented here were obtained using the HARPS échelle spectrograph at the 3.6-m telescope at La Silla Observatory. HARPS is a stabilized high-resolution fibre-fed spectrograph that operates in the visible range (380–680 nm) with a resolving power of $R \sim 110\,000$. The reported 0.8–0.9 m s^{-1} RV long-term stability limit (Pepe et al. 2011), also on M dwarfs (Anglada-Escudé & Butler 2012), makes it currently the most suitable spectrograph for this project.

The GJ 588 and GJ 699 high-cadence data were obtained during a CTB observational campaign carried out in 2013 May (see the time series of the targets observed during this run in Fig. 2, the black squares and red dots account for GJ 588 and GJ 699, respectively). We monitored GJ 588 during four consecutive nights. On the contrary, we observed GJ 699 during three nights taken immediately before and after the GJ 588 observations (two consecutive nights were taken before and one was observed after). In total, we obtained 189 and 108 spectra for GJ 588 and GJ 699, respectively. The exposures times were ∼600 s for GJ 588 and either 500 or 600 s for GJ 699. Among other observational parameters, we got, respectively for GJ 588 and GJ 699, maximum airmasses of 2.2 and 2.0, mean signal-to-noise ratios (SNRs) of 63.1 and 62.8 and mean seeing values of 1.03 and 0.64.

The spectra were extracted and wavelength calibrated with the standard HARPS Data Reduction Software (DRS). We used the Template Enhanced Radial velocity Reanalysis (TERRA) software to calculate the RVs, since it has demonstrated to be more accurate on M dwarfs (Anglada-Escudé & Butler 2012). Additionally, we also calculated a proxy of the mean-line profile of the spectra. In particular, instead of using the cross-correlation functions given by the HARPS pipeline, we calculated them using a least-square

deconvolution (LSD) technique (Donati et al. 1997). See more details in Section 3.4.

3 INSTRUMENTAL EFFECTS CORRECTION

The analysis of the CTB data revealed both intranight (Berdiñas et al. 2016) and possibly night-to-night instrumental effects that need to be mitigated when dealing with high-cadence observations.

3.1 Wavelength calibration jumps

One of the effects that we quickly identified in other CTB data were night-to-night RVs jumps of ∼0.5–2.0 m s^{-1}. The stability of the RVs obtained with TERRA or any other reduction software relies on the calibration of the wavelength, which, in HARPS, is given by a Th–Ar hollow cathode lamp (HCL) measurement taken at the beginning of each night. Since the wavelength solution has also an associated uncertainty, its random errors are bound to produce night-to-night jumps that can easily reach a ∼1–2 m s^{-1} level. Moreover, compared to the typical G and K dwarfs for which HARPS was designed, M-dwarf stars have most of the flux and Doppler information in the redder part of their spectra and hence of the detector. As a result, night-to-night RVs become more sensitive to random errors in a smaller number of the redder diffraction orders. To calculate the night-to-night offsets in the wavelength solution, we first selected one GJ 699 spectrum per night. For nights with several GJ 699 spectra we selected the ones observed early after the beginning of the night (t_i). Then, we obtained the Doppler drift of the wavelength solution between nights as

$$\text{drift} = c\left(\left\langle \frac{\lambda_{t_i}}{\lambda_{t_0}} \right\rangle - 1\right) \text{ (m s}^{-1}\text{)}, \quad (1)$$

that is, referenced to the first GJ 699 spectrum of the run (t_0). Here, λ accounts for the wavelength of each pixel in the 22 reddest spectral orders and c is the speed of light.

As a complementary wavelength reference source, a spectrum with a stabilized Fabry–Pérot (FP) interferometer is also obtained as part of the calibration procedure executed before the observing night starts.[2] Using TERRA, we computed the RV drift of these FP frames against the FP frame taken in the first epoch. In the upper panel of Fig. 3, we compare the nightly FP and wavelength solution drifts. The data points of the wavelength solution and FP do not have the same time stamp (i.e. they do not match in the x-axis of Fig. 3) because while the FP is recorded before the start of the night, the GJ 699 spectra used to obtain the wavelength solution were observed throughout the night. Nevertheless, we can still compare both drifts because a single calibration procedure is typically used as reference for all the observations of the night. Results indicate that even when the FP measurements show some structure, its corresponding time series is much more stable (Δ_v(rms) = 0.22 m s^{-1}) than in the case of the wavelength solution (Δ_v(rms) = 1.16 m s^{-1}). Although they are likely to contribute to random noise over long time-scales, the jumps in the wavelength solution already cause serious issues in the consistency of our time series in the high-cadence domain (signals in the $P < 2$ d range). For example, we can see in Fig. 3 how a 3.6 m s^{-1} jump in the wavelength solution causes the drift of the GJ 588 RVs between the first and the second night. As a comparison, the time series of GJ 588 looks much flatter if we use, instead of the individual night calibrations, the wavelength solution of the first night for all the observations (compare black and grey squares in the bottom panel of Fig. 3).

[2] The FP frames were taken in the fibre B while the spectrum of the Th–Ar hollow cathode lamp was recorded in the fibre A.

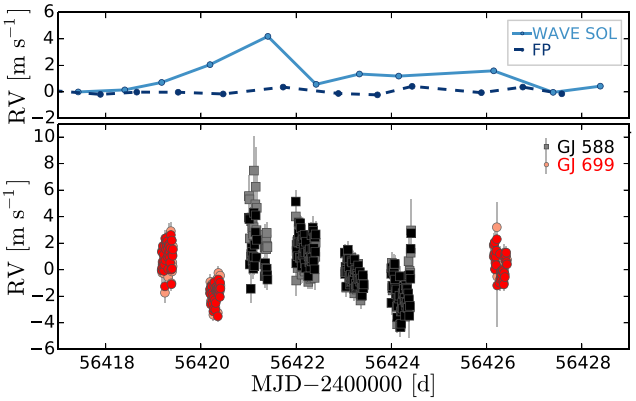

Figure 3. Upper panel: comparison of the stability of the wavelength solution (light blue solid line) and Fabry–Perot (dark blue dotted line). The wavelength solution, which relies on the Th–Ar hollow cathode lamp, is less stable. Bottom panel: the dark colour symbols indicate RVs obtained for the same wavelength solution while the light colour refers to RVs from individual night calibrations. The squares and dots correspond to GJ 588 and GJ 699, respectively.

This random variability of the wavelength solution is one of the causes of the spurious ∼1-d peaks (and integer fractions of it, like 1/2 and 1/3) that commonly appear in the periodograms of high-cadence data (e.g. the low frequency excess in the power spectra of fig. 3 and fig.7 of Bedding et al. 2007 and Bouchy et al. 2005, respectively). Although we do not expect pulsations at such long periods, the window function can inject significant correlated noise at other frequencies, which is undesirable. We use the strategy of using a common wavelength solution for all the run to mitigate this source of noise. The long-term stability of the FP (>week) has not yet been established (Pepe & Lovis, private communication) so we advise against using this technique to improve the consistency of time series with a time span longer than a few days.

3.2 Charge transfer inefficiency

Doppler shifts have been reported to correlate with the SNR of the observations (Bouchy et al. 2009). This is in part due to the charge transfer inefficiency (CTI) effect. The CTI gets worse at low fluxes (i.e. at low SNRs) and it is associated with an inefficient transference of charge between adjacent pixels during the readout process in charge-coupled devices (CCD). The CTI can produce effective changes in the position and the shape of the HARPS spectral lines (Lo Curto et al. 2012; Zhao et al. 2014), and thus, cause RV offsets of several m s^{-1}(Bouchy et al. 2009) for measurements with SNR below 30–40. Bouchy et al. (2009) proposed a method to assess the charge lost in the pixels of the SOPHIE spectrograph (Perruchot et al. 2008). Using similar methods, the raw frames of HARPS-N are corrected for CTI since 2013. However, such a correction was not implemented in HARPS (Lovis & Pepe, private communication).

To mitigate CTI effects for our campaign, we implemented an empirical post-processing correction: during a CTB campaign carried out in 2014 December we observed GJ 887, a very bright M2V spectral type star, with different exposure times, i.e. at different SNRs. Similarly to what Santerne et al. (2012) did for SOPHIE, we

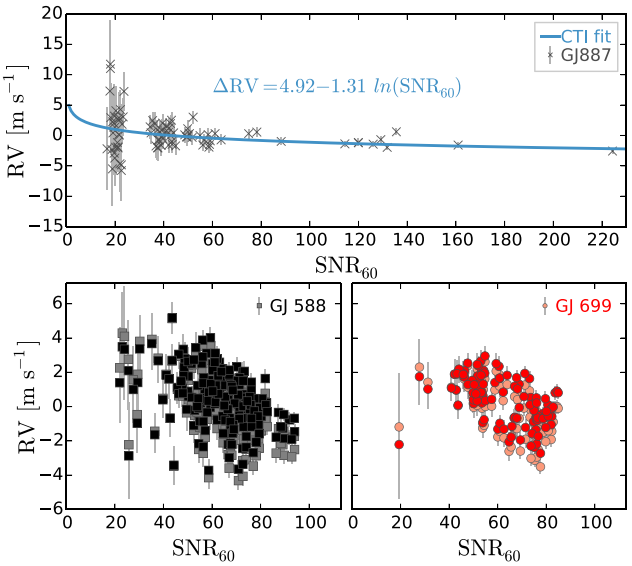

Figure 4. Upper panel: GJ 887 RVs obtained at different exposure times (from 10 up to 600 s), i.e. for a range of SNRs. This experiment was done to monitor the CTI effect that distorts the RV at low SNR and to get the CTI calibration function (blue solid line and function). Bottom panels: the light symbols are the original RVs of GJ 588 (left; squares) and GJ 699 (right; dots), while the dark markers correspond to their CTI-corrected counterparts.

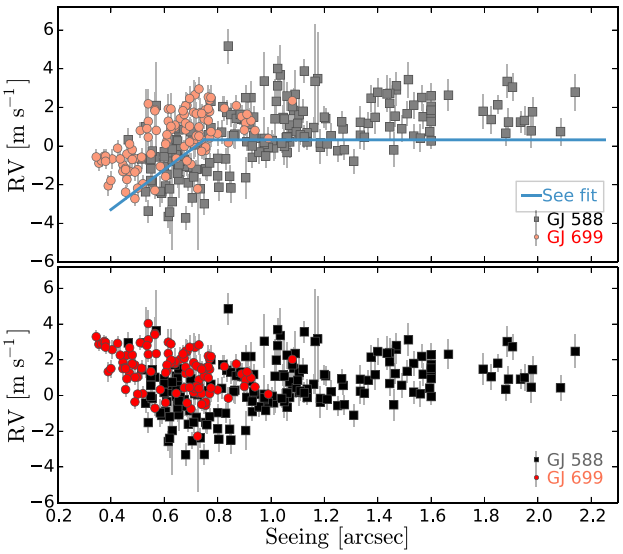

Figure 5. Seeing effect. Upper panel: GJ 588 (grey squares) and GJ 699 (light red dots) RVs uncorrected from the 'seeing effect'. The RVs decrease for the data points observed at seeing values lower than the HARPS fibre size, i.e. 1 arcsec. Based on dispersion criteria, we only applied a linear fit to the RVs below 0.75 arcsec. Corrected series are shown at the lower panel with dark colours (black for GJ 588 and red for GJ 699).

fit a relation between RV and SNR that is valid for, at least, M-dwarf stars observed with HARPS. This is

$$\Delta \mathrm{RV} = 4.92 - 1.31 \ln \mathrm{SNR}_{60}\,(\mathrm{m\,s^{-1}}), \quad (2)$$

where SNR_{60} refers to the SNR measured in the spectral order 60. In Fig. 4, we show the CTI empirical calibration function in the upper panel and the corrected RVs in the lower part. There are other effects that cause the RVs to correlate with the SNR. An example is the 'the colour effect' outlined in Bourrier & Hébrard (2014). Contrary to the CTI, which only affects measurements with SNR below 30–40, these effects can cause trends for the whole range of SNRs as we see in the lower panels of Fig. 4.

3.3 Seeing effect

We observed that when atmospheric conditions were excellent (i.e. seeing <1 arcsec), the Doppler measurements of several stars were correlated with lower values of seeing (see Fig. 5). Such an effect, known as the 'seeing effect', was well described by Boisse et al. (2010a,b), and it was pointed out as the main limiting factor of the SOPHIE spectrograph (Perruchot et al. 2008). The effect can be understood as vignetting of the telescope pupil. Boisse et al. (2010a) explained how this vignetting translates into light pattern variabilities at the output of the optical fibre linking the telescope and the spectrograph (in particular, into changes of the far-field image of the fibre); and how this finally produces small shifts of the spectral lines (i.e. of the RVs). HARPS has a double image scrambler to stabilize the image and to homogenize the illumination. Since this system interchanges the fibre near and far fields, vignetting the pupil results equivalent to reduce the size of the image of the star. That is, equivalent to have good seeing conditions. When the seeing is below 1 arcsec the telescope image is sharper than the HARPS fibre width, and thus, if the scrambling is not perfect, the far-field changes cause RV shifts up to $\sim$3 m s^{-1} (Boisse et al. 2010a).

In 2013, Bouchy et al. (2013) showed how to partly correct the 'seeing effect' of SOPHIE. They demonstrated that using linking fibres with octagonal-shaped cores, instead of circular ones, improves the scrambling efficiency and the resulting RV precision by a factor of $\sim$6. In 2015 May an octagonal fibre link was introduced in HARPS. However, the data used in this study were obtained before this instrumental update. Therefore, we applied a post-processing empirical correction based on our observations.

We used as a proxy for the seeing the value given in the data headers that is obtained as the full width at half-maximum (FWHM) of the acquisition image taken by the guider camera. Then, we fitted and subtracted a linear function to the observations with seeing <0.75 arcsec (see Fig. 5). This value is below the HARPS fibre width (1 arcsec) and was chosen in terms of the variability observed in the 2013 May data. Moreover, our 0.75-arcsec cut-off resulted to be in good agreement with the 0.7 arcsec quality image given by the 3.6-m telescope where HARPS is installed (Boisse et al. 2010a).

3.4 The SED normalization effect

Our previous studies using CTB high-cadence data revealed systematic effects within the night in HARPS-N (Berdiñas et al. 2016). Such systematic effects, dubbed 'SED normalization effect' (where SED stands for spectral energy distribution), consist in wavelength dependence of the flux losses caused by small illumination changes at the fibre entrance.

After calculating the pseudo-SED function following Berdiñas et al. (2016), we detected wavelength and time dependencies in the flux distributions of GJ 588 and GJ 699 (see Fig. 6). Thus, the HARPS-DRS pipeline does not account for the 'SED normalization effect', neither for HARPS nor for HARPS-N. This implies that the mean-line profile proxies given by the DRS (i.e. the cross-correlation function, or CCFs) are uncorrected, and so the indices derived from them.

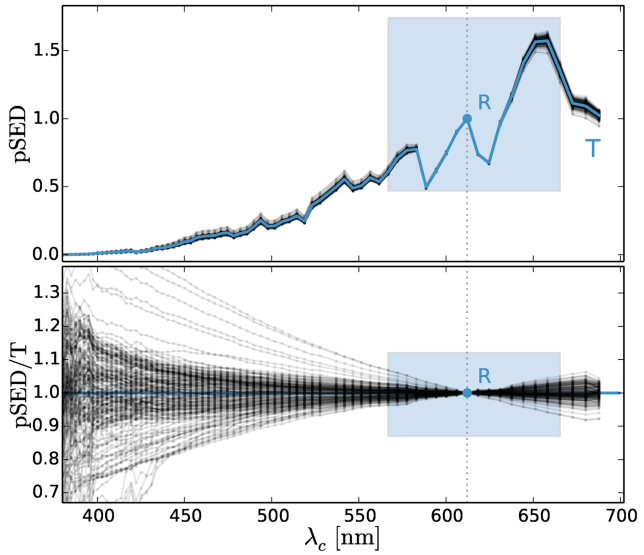

Figure 6. Upper panel: GJ 588 pseudo-spectral energy distribution (or pSED), calculated as the sum of the flux at each spectral order normalized by the flux at order-60. The pSED is plotted versus λ_c, the central wavelength of each spectral order. R indicates the central wavelength at order-60. Lower panel: the pSEDs normalized by T, the averaged pSED of the run (see blue line in the upper panel). The index κ measures the relative changes in the slope of the pSEDs. It is calculated for the range of wavelengths within the blue area (see Berdiñas et al. 2016 for more details).

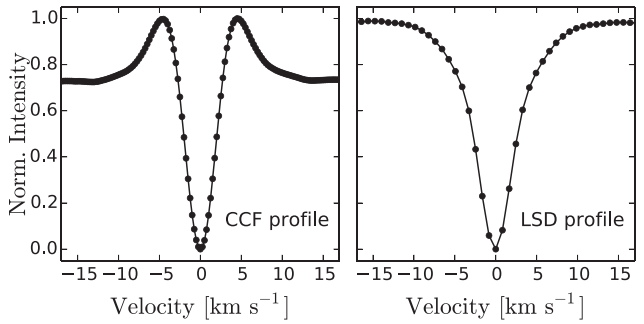

Figure 7. Comparison of a CCF profile obtained from the DRS pipeline (left-hand panel) and a profile obtained with a LSD approach (right-hand panel). The profiles correspond to the same GJ 588 spectrum, and were shifted to zero-velocity and normalized by its minimum intensity for a better visualization.

Thus, in order to measure uncontaminated mean-line profiles we have to correct their variable slope. To this end, we re-scaled the flux at each order and epoch to match that of our template spectrum (with highest SNR). Once we corrected the spectra from the 'SED normalization effect', we calculated the mean-line profile with a LSD approach (Donati et al. 1997) as outlined in Barnes et al. (1998, 2012). Compared to the CCFs from the DRS, our LSD approach resulted in smoother mean-line profiles. As a proof of that, in Fig. 7 we show a CCF and a LSD mean-line profile for the same GJ 588 spectrum. The side lobes present in the CCF profile[3] increase the uncertainty of the Gaussian fit and of any other

[3] Side lobes are generally caused by blending between nearby lines. This is typical of cool stars that are crowded with lines that distort the star's continuum.

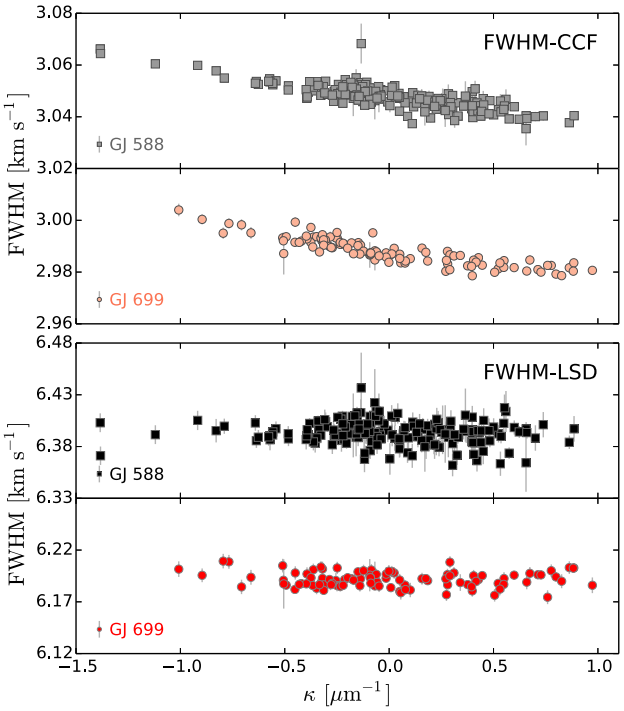

Figure 8. SED normalization effect. FWHM-CCF (upper panels; light colours) and FWHM-LSD indices (lower panels; dark colours) plotted versus κ that accounts for flux variabilities of the SED. The squares and dots correspond to GJ 588 and GJ 699, respectively. The FWHM-CCF and the FWHM-LSD correspond, respectively, to the FWHM of the Gaussian function fitted to the cross-correlation functions by the DRS and to our colour-corrected least-squares deconvolution profiles.

parameters derived from it, such as the FWHM (the line width), the RV (the line centroid) and the bisector (BIS; the line asymmetry).

The LSD method consists in finding the convolution kernel applied to a list of lines to reproduce the observed spectrum in a least-squares sense, thus naturally accounting for the line blends. To create such a list of lines, we used a co-added high-SNR spectrum generated with all the observations. This processing consists in matching the continuum and Doppler shift of each spectrum to the highest SNR spectrum, and then co-adding all of them. When selecting lines for the LSD, chromospheric emission lines (such as Hα and Na I D1 and D2 lines) or any telluric lines deeper than 0.05 compared to the normalized continuum are excluded. The LSD profile is obtained using only the reddest HARPS apertures (from order 32 to 72) and it is sampled at 0.821 km s^{-1}, which matches the effective average pixel size of HARPS (the DRS oversamples the pixel size using velocity steps of 0.25 km s^{-1}).

Then, for each LSD profile in absorption, we produce a normalized positively defined probability distribution function by subtracting their residual continuum (see section 4.2.2 in Berdiñas et al. 2016) and normalizing its area to unity. Finally, we calculate the FWHM-LSD index as the FWHM of a Gaussian function fitted to the mean-line profiles. The FWHM-LSD is a proxy of the changes of the profile width. In Fig. 8 we show how, in contrast to the FWHM of the CCFs (FWHM-CCFs), the FWHM-LSD measurements do not correlate with the changing slope of the observed SEDs. That is, with the index κ that accounts for the SED slope change in linear region (see blue area in Fig. 6). Both indices, the FWHM-CCF and the FWHM-LSD resulted to have different mean values. The side lobes of the CCFs may necessarily derive in an underestimation of

Table 2. GJ 588 and GJ 699 RV and FWHM data used in this study. The columns are: the star, the Barycentric Julian Date (BJD), the observed radial velocities obtained with TERRA (RV), the observed FWHM index obtained from the cross-correlation function by the HARPS pipeline (FWHM-CCF), the radial velocities corrected from the instrumental effects as described in Section 3 (RVc) and the FWHM corrected from the SED normalization effect (FWHM-LSD). This study analyses the data of the last two columns.

Object	BJD (d)	RV ($m\,s^{-1}$)	FWHM-CCF ($m\,s^{-1}$)	RVc ($m\,s^{-1}$)	FWHM-LSD ($m\,s^{-1}$)
GJ 588	56421.518	5.55 ± 1.61	3046.74 ± 3.87	3.36 ± 1.52	6413.88 ± 19.79
GJ 588	56421.528	5.30 ± 1.66	3046.01 ± 4.91	3.04 ± 1.50	6396.19 ± 23.49
GJ 588	56421.533	2.36 ± 0.88	3049.73 ± 2.07	0.30 ± 0.76	6395.80 ± 13.58
GJ 588	...	...	...	...	...
GJ 699	56419.682	0.00 ± 0.75	2981.66 ± 1.77	−0.15 ± 0.61	6203.06 ± 6.08
GJ 699	56419.688	1.42 ± 0.86	2982.55 ± 1.75	1.23 ± 0.72	6200.08 ± 6.06
GJ 699	56419.694	−0.24 ± 0.78	2984.66 ± 1.78	0.07 ± 0.56	6197.53 ± 6.12
GJ 699	...	...	...	...	...

Note. This table is available in its entirety in a machine-readable form in the online journal. A portion is shown here for guidance regarding its form and content.

the continuum, and so of the FWHM of the Gaussian fitted to the CCFs by the DRS.

Uncertainties in the LSD profiles, and thus in the FWHM-LSDs are difficult to estimate analytically. Instead, we used an empirical procedure based on the fact that uncertainties follow the SNR of the observations. We assumed the standard deviation of the differences between FWHM-LSD data points to be $\sqrt{2}$ times the uncertainty of the mean SNR of each night (at reference échelle aperture number 60). We used as reference the first observation of each night, then the error values of the observations within the night were obtained by scaling this standard deviation by a factor of $<SNR>/SNR_{obs}$.

The final measurements to be used for this study were the RVs and the FWHM-LSDs corrected as explained above. See Table 2 for the original and corrected data (full version included in the online material). In Fig. 9 we show the final resulting time series. The FWHM-LSD still shows some patterns that seem to repeat themselves on different nights (e.g. the arc shape of the FWHM-LSD in nights 2 and 3 of GJ 588). Since we have corrected the spectra from the SED normalization effects, such variability cannot be driven by flux distribution changes. An explanation could come from the barycentric broadening of the spectral lines caused by changes of the star–Earth differential velocity during the observations. That is, by changes in the star–Earth relative RV between observations taken close and far from the zenith.[4] However, our measurements indicate that the contribution of such effect is negligible at the HARPS precision level for these targets. Nevertheless, even when we cannot identify the origin, we know that the periods associated with such pattern will be close to 1 d and/or submultiples in the periodograms. Therefore, our study ranging from 20 min to 3 h precludes any misleading signals coming from this pattern.

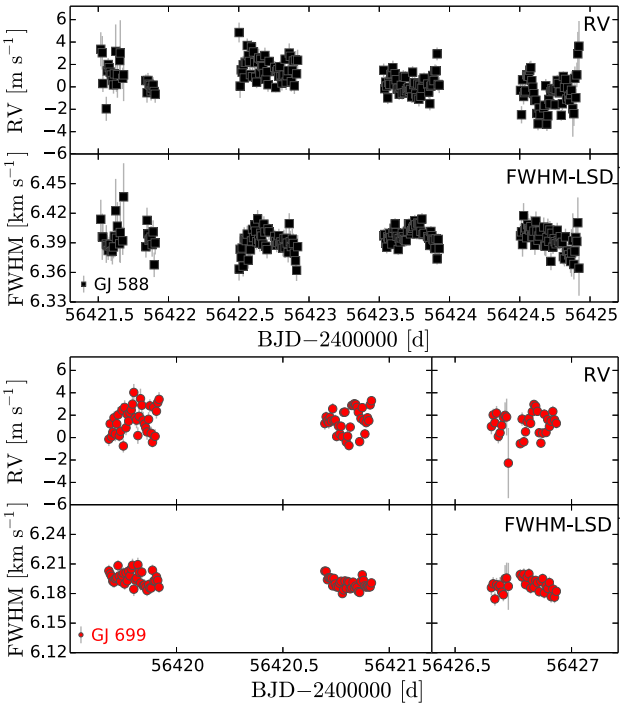

Figure 9. RV and FWHM-LSD time series used in this study and resulting after applying several intranight and night-to-night corrections. The upper and bottom panels show the four and three high-cadence observing nights of GJ 588 (black squares) and GJ 699 (red dots), respectively. The last GJ 699 observed night was four nights after the second.

4 ANALYSIS

4.1 Short time domain variability

We used periodograms to search for periodic signals embedded in the RV and FWHM-LSD high-cadence time series. Periodograms are plots that represent a reference statistic in the *y*-axis versus a range of periods in the *x*-axis. This reference statistic accounts for the improvement of fitting the data with a sinusoidal model compared to an initial hypothesis (e.g. no periodic signals). Classic Lomb–Scargle periodograms (Lomb 1976; Scargle 1982) use the F-ratio reference statistic; instead, we used the difference of the logarithm of the likelihood function as the reference statistic ($\Delta \ln \mathcal{L}$ periodograms; see Baluev 2009). Compared with the Lomb–Scargle periodograms, the likelihood periodograms have several advantages. The most important one is that the likelihood function allows a *global* search, in the sense that all parameters (including noise parameters such as the 'stellar jitter') are optimized at the period search level. This is especially important in the case of M dwarfs, which are all affected by activity to a certain extent.

[4] Bodies at the zenith seem to move faster for a fixed observing time causing a broadening of the spectral lines.

For a grid of periods uniformly sampled in the frequency space our likelihood periodograms search the model best fitting the data. We defined this model as

$$v_{i,\mathrm{Night}} = \gamma_{\mathrm{Night}} + \dot{\gamma}(\Delta t_i) + \mathcal{K}_p(\Delta t_i), \quad (3)$$

where γ_{Night} and $\dot{\gamma}(\Delta t_i)$ are parameters accounting for an offset velocity and a linear trend, respectively. Note that we let each night have a different velocity offset, whereas a single linear trend is fitted to all nights. This means we have modelled the Doppler time series considering each high-cadence night as an independent set. The analysis procedure is equivalent to that used in Anglada-Escudé et al. (2016a), where we considered different instruments as independent data sets. We proceeded in that way aiming at filtering out any possible periodicity longer than 1 d in which we were not interested when searching for M dwarfs stellar pulsations. The 1-d signals typically populate periodograms and, even when we have made an effort to correct our data from nightly jumps (see Section 3), this is also the case here. Most probably other unknown intranight systematic effects drift the RVs during the observations causing these 1-d periods and/or submultiples. In other words, our approach prevents a superposition of pth sinusoids that otherwise would be needed in the model before we were able to study sinusoids compatible with the pulsation range of interest. As a comparison, we show in the appendix the result when all nights are analysed as a single data set. On the other hand, the linear trend parameter allows to account for possible long trends caused by a long-term acceleration. Finally, $\mathcal{K}_p(\Delta t_i)$ is a sum of k sinusoids and can be written as

$$\mathcal{K}_p(\Delta t_i) = \sum_{p}^{k} A_p \sin\left(\frac{2\pi}{P_p} t_i\right) + B_p \cos\left(\frac{2\pi}{P_p} t_i\right), \quad (4)$$

where each pth sinusoid is defined by the A_p and B_p amplitudes and the period P_p. As we said, the likelihood periodograms allow a *global* search, and that means we do not apply pre-whitening procedures. Instead, every time that a model with p+1 sinusoids (SOLp+1) is preferred over the p case (SOLp) a new sinusoid is added to the model. Then, all the model parameters are re-adjusted every time that we search for those with the new added sinusoid. With this model we are assuming that stellar pulsations can be modelled with sinusoidal functions. This assumption can be untrue, but this is the simpler model we can apply in the absence of information about the real nature of the M dwarfs stellar pulsation signals. Moreover, similar models have demonstrated to be useful in the search of pulsations in other spectral types. For more details about the model see Anglada-Escudé et al. (2016a).

The second and third panels of Fig. 10 show the RV and FWHM-LSD likelihood periodograms of GJ 588. The same panels of Fig. 11 show the likelihood periodograms for GJ 699. Grey areas in these panels highlight the range of frequencies where pulsations are not expected (i.e. periods out of the 8–72 d^{-1} frequency range). In the upper right-hand corner of these panels we indicated the number of p sinusoids included in the model until the first solution outside the grey area is found. For example, the SOL2 in the upper right-hand corner of the second panel of Fig. 10 means the model fitting the RVs of GJ 588 contains two sinusoids, the first one corresponding to a large amplitude signal with a period out of the 20 min–3 h range. In particular, the periods of these sinusoids were: in the case of the RVs of GJ 588 ∼0.5 d (SOL1), for FWHM-LSDs of GJ 588 ∼1 and ∼0.4 d (SOL1 and SOL2) and ∼0.3 d (SOL1) in the case of the FWHM-LSD of GJ 699.

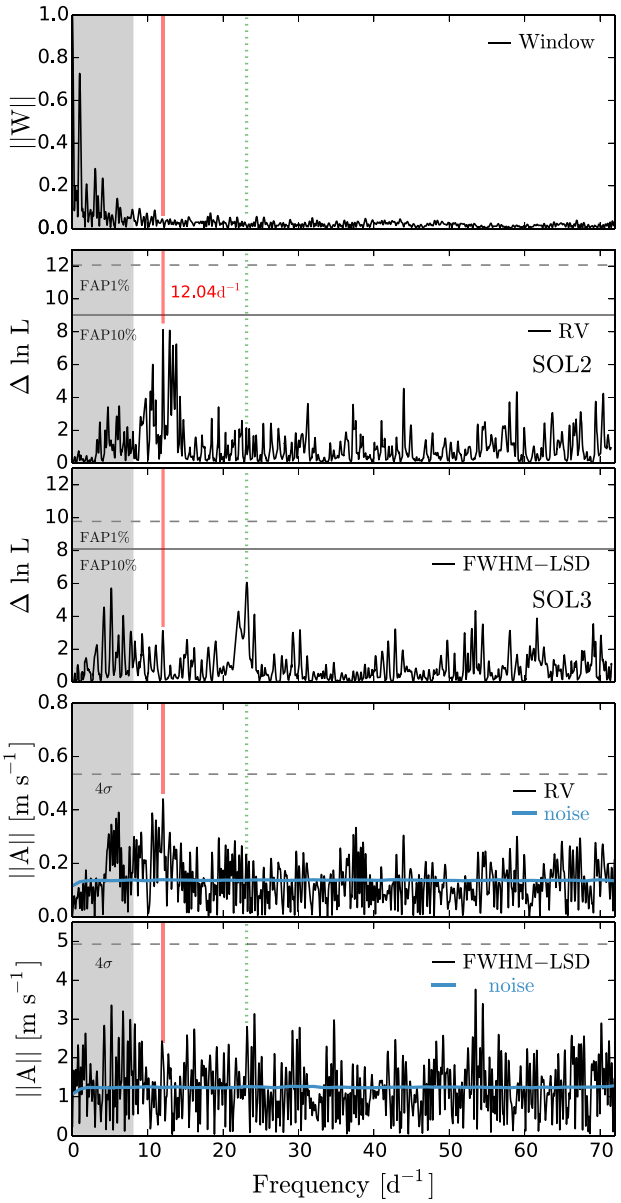

Figure 10. GJ 588 analysis of periodicities. GJ 588 window function (first panel), RVs and FWHM-LSD likelihood periodograms (second and third panels) and RVs and FWHM-LSD power spectra (fourth and fifth panels). The grey areas indicate frequencies out of the predicted pulsational range. The vertical red line highlights a putative signal at 12.04 d^{-1} appearing in both the RVs likelihood periodogram and power spectra. The vertical dotted green line highlights a peak found in the RVs of GJ 699 for which we detect a counterpart in the FWHM-LSDs of GJ 588 (third panel). Horizontal lines account for different levels of significance. The blue lines in last two panels indicate the noise power spectra. See main text for details.

As a figure of merit to quantify the significance of a detection we used the so-called 'false alarm probability' (FAP), which accounts for the probability of obtaining a peak by a random combination of the noise (Cumming 2004). A FAP = 1 per cent is considered the minimum threshold that a peak has to reach to claim it as a detection (Cumming 2004; Baluev 2009). The grey dashed lines in the likelihood periodograms of Figs 10 and 11 highlight the 1 per cent FAP thresholds. As a comparison, the 10 per cent FAP is also shown with a solid line. The FAP can be calculated analytically,

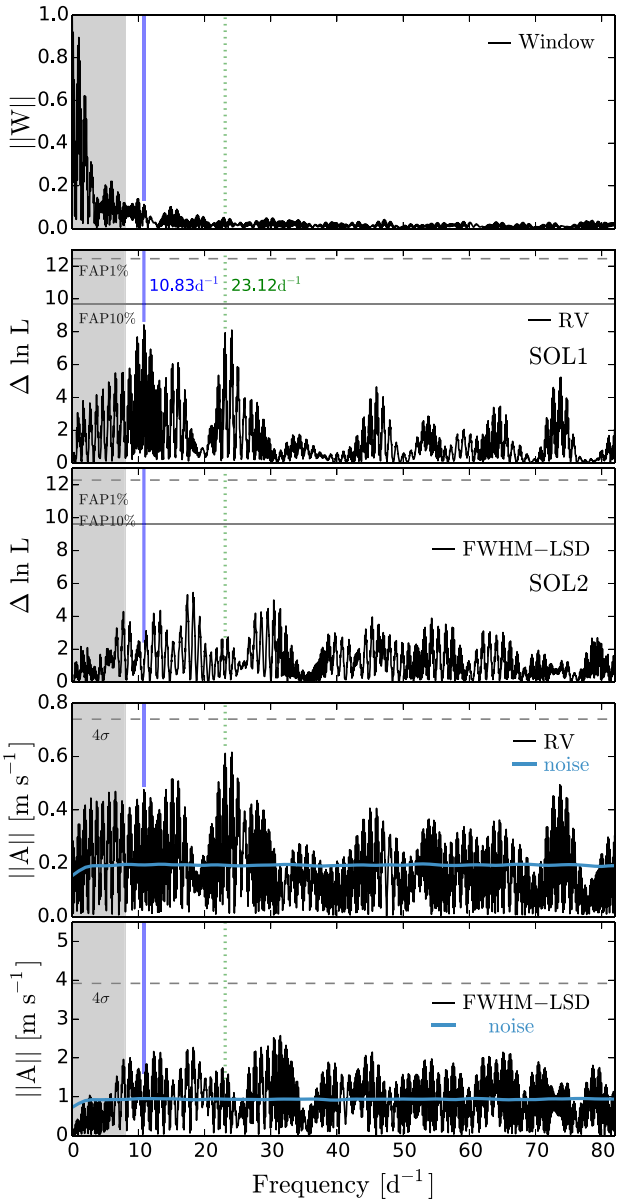

Figure 11. GJ 699 analysis of periodicities. Panels follow the same criteria as in Fig. 10. The interruption of the continuous consecutive night monitoring complicates the window function causing aliases. Like for GJ 588, no significant signals were detected, but some non-negligible structure is present. The two preferred peaks are at 10.83 d^{-1} (vertical blue line) and at 23.12 d^{-1} (vertical dotted green line) also present in the FWHM-LSD periodogram of GJ 588.

but it is required the number of independent frequencies in the range of study. Given that this number is ambiguous when the sampling is not regular, we estimated the FAP empirically. The goal was to establish how the maximum likelihood statistic is distributed in the presence of noise only. To do this, we generated synthetic data by randomly permuting the measurements among the given observed epochs (i.e. we bootstrapped the time series). Then we calculated periodograms over the resulting series and we recorded the maximum $\Delta \ln \mathcal{L}$ achieved in each of these test periodograms. The FAP of a signal is the number of synthetic experiments giving spurious $\Delta \ln \mathcal{L}$ larger than the original time series divided by the total number of tests. Thus, after repeating this experiment $N = 10^3$ times, the highest $\Delta \ln \mathcal{L}$ obtained was made to correspond to a 0 per cent FAP. From this assumption we can easily derive the 0.1, 1 and 10 per cent FAP thresholds as we show in Fig. 12. That is, plotting the maxima $\Delta \ln \mathcal{L}$ sorted increasing order versus n/N, the cumulative number of experiments and interpolating the result.

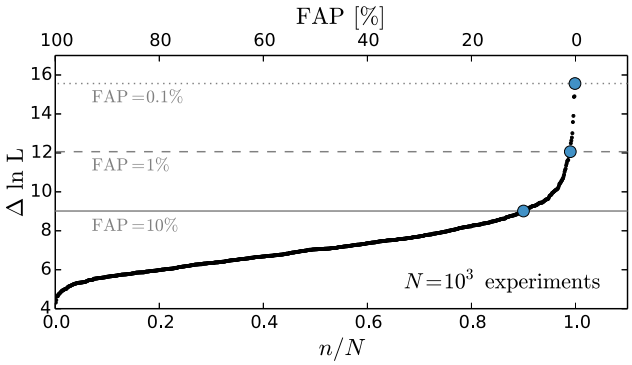

Figure 12. Bootstrapping approach used to calculate the FAP thresholds. The *y*-axis corresponds to the maximum $\Delta \ln \mathcal{L}$ values resulting for each of the $N = 10^3$ bootstrapping experiments we performed. The *x*-axis accounts for n/N, the cumulative probability of obtaining a certain $\Delta \ln \mathcal{L}$ (i.e. the $\Delta \ln \mathcal{L}$ values are sorted and then plotted versus n/N). The highest $\Delta \ln \mathcal{L}$ obtained corresponds to the lowest false alarm probability (FAP = 0 per cent) and the other values are obtained from this assumption. Horizontal lines and blue dots indicate the 0.1, 1 and 10 per cent FAP thresholds. This experiment corresponds to the RVs of GJ588, i.e. these are the FAP thresholds plotted on the second panel of Fig. 10.

No signals were found with a FAP <1 per cent in the range of frequencies where we expected to find pulsations. However, for the RVs, we can see some excess of power for both targets, GJ 588 and GJ 699, in the range of a few hours (or tens of d^{-1}) close to the 10 per cent FAP. In particular, the preferred peaks have a corresponding frequency of 12.04 d^{-1} (indicated with a vertical solid red line in Fig. 10) in the case of GJ 588, and of 10.83 and 23.12 d^{-1} (vertical solid blue and dotted green lines in Fig. 11) in the case of GJ 699. Nevertheless, the presence of the 23.12 d^{-1} peak also in the FWHM-LSD periodogram of GJ 588 (highlighted in Fig. 10 also with a vertical dotted green line) lead us to suspect that it could be an instrumental artefact. The 12.04 d^{-1} is recovered regardless of the approach used to filter out the periodicities close to 1 d (and their aliases). However, we decided to consider each night as independent data sets because in this case the model requires fewer sinusoids.[5] The FWHM-LSD periodograms do not present any other peak besides the suspected spurious at 23.12 d^{-1} for GJ 588, and a peak at 53.5 d^{-1} that we think is an artefact since it arises in the power spectra but not in the likelihood periodogram. But, even when some structure is present, any peak is not even close to the permissive threshold of 10 per cent FAP, for either GJ 588 or GJ 699.

In order to perform an independent assessment of the possible signals, we have also computed the power spectra using the code SIGSPEC (Reegen 2007). This code uses a pre-whitening methodology, i.e. it does not globally model all the solutions. As a consequence, in this case we used as input the time series of the residuals to the best models found with the likelihood periodograms, so as not

[5] For example, in the case of GJ 588 RVs if we consider each night independently only one sinusoid is required to account for the long-term variability (SOL1 corresponds to ∼0.5 d). On the contrary, if we consider the run as a whole, the 12.04 d^{-1} period is recovered after fitting two ∼1.5 and ∼0.5 d sinusoids. See the appendix for more details.

to introduce any undesirable trend as a result of the pre-whitening process of signals in the day or sub-day range (see Anglada-Escudé & Tuomi 2015 for more details). Thus, we used the residuals to SOL1 (∼0.5 d) for the RVs and to SOL2 (∼1 and ∼0.4 d) for the FWHM-LSD of GJ 588; and in the case of GJ 699, the original RVs and the residuals to SOL1 (∼0.3 d) for the FWHM-LSD. The power spectra rely on the discrete Fourier transform (DFT) and consist of plotting its amplitude (or the square root of the sum of its real and imaginary squared components) versus a grid of frequencies. The last two panels of Figs 10 and 11 show the RV and FWHM-LSD power spectra. The general criterion to consider a peak statistically significant in a power spectra is to reach at least four times the signal/noise amplitude ratio (Breger et al. 1993). This rule is the commonly known as the '4σ criterion'. Note that, besides the name, this concept is not directly the probability of a normal distribution. Statistical conclusions that attach to regular spaced time series do not apply to non-equally sampled data as is the case of our observations. The grey dashed lines in the last two plots indicate the 4σ threshold. It was calculated as four times the mean amplitude of the peaks with frequencies higher than 8 d^{-1} (white area, pulsation range). Again, even when no peak reaches the threshold, we obtained a power excess in the range of a few hours with a preferred peak at 12.04 d^{-1} in the RVs of GJ 588. In the same way, the power spectra of GJ 699 showed results comparable to those of the likelihood periodograms.

We also calculated respective window functions (first panel of Figs 10 and 11) using a DFT. This function helps to identify misleading peaks arising from periodicities caused only by the sampling. The reason for the more complicated window function for GJ 699 is the time gap between the second and the third observing night that causes more aliases. However, since the resolution of the individual peaks is inverse to the total time baseline, this is also the reason why in the GJ 699 periodogram the peaks are narrower. Additionally, the window function is a very useful tool because any peak corresponding to a real periodic signal in the time domain, rather than being a simple Dirac delta function in the power spectra, is a convolution of it with the window function (Gray & Desikachary 1973). In this case, the window function also indicates that the putative signal at 12.04 d^{-1} in the case of GJ 588 is far away from the range of influence of the window peaks.

Aiming at checking if the sampling could originate an excess of power in a certain zone, we have also generated the power spectra of the noise. That is, we calculated the averaged power spectra resulting from 10^3 bootstrapping experiments. Such power spectra were found to be almost flat, indicated by the horizontal blue lines of the bottom panels of Figs 10 and 11. This result means that the sampling does not bias the spectrum of the noise in the absence of signals. Therefore, even when the 12.04 d^{-1} or the 10.83 and 23.12 d^{-1} peaks do not reach our threshold criterion, the sampling does not seems to be the cause.

4.2 Compatibility with pulsation models

The discussed putative signals may be caused by intrinsic oscillations of the star that might not be necessarily described as single frequency sinusoids. Therefore, as a first step, we have calculated where we could expect to find pulsations with these putative periods in the Hertzsprung–Russell (HR) diagram. This approach will allow us to know if excited models are compatible with the star parameters, i.e. if the star and any excited model with similar physical parameters share the same position in the HR diagram. With this aim, we used the evolutionary tracks from RL14, which were calculated from different models with a range of masses of 0.10–0.60 $M_\odot$ with 0.05 resolution (see more details about these models in table 1 from RL14). Later, we perturbed models along these tracks and we explored their pulsation instabilities for modes of degree $\ell = 0$–3.

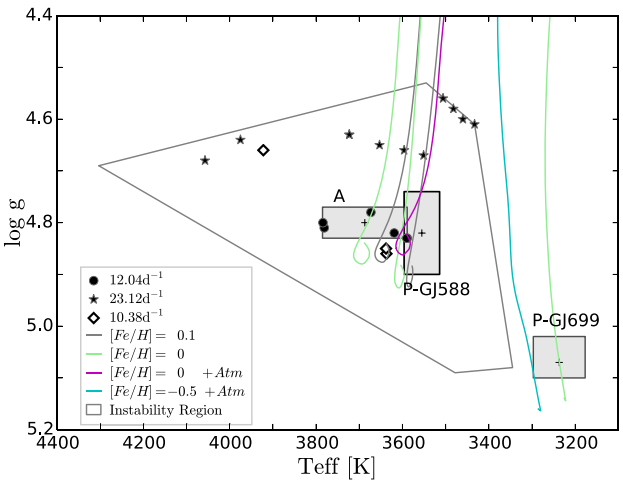

Figure 13. Photometric (P-GJ 588 and P-GJ 699) and asteroseismic (A) boxes in the $T_{\rm eff}$–log g diagram. We only plotted the evolutionary tracks in RL14 that cross any of these boxes and have metallicities and masses closer to the literature values (0.40 and 0.45 M⊙ and supersolar metallicity for GJ 588, and 0.15 M⊙ and subsolar for GJ 699). Solar metallicity was also included for comparison purposes. Stellar models including an atmosphere are indicated with the label 'Atm' in the legend. All tracks were calculated with a mixing length parameter $\alpha = 1$. Solid black dots indicate models excited with a 12.04 d^{-1} period (putative signal of GJ 588). Stars and diamonds correspond to models with 23.12 and 10.38 d^{-1} periods (putative signals of GJ 699). The black dot in the intersection of the A and P-GJ 588 boxes (0.45 $M_\odot$ on the magenta track) gives theoretical support to the GJ 588 putative signal.

In Fig. 13 solid black dots show the stellar models excited with periods in the range of the observed one for GJ 588 (∼12 d^{-1}). The physical parameters of those excited models set up the 'asteroseismic box' of GJ 588 (see A box in Fig. 13 defined by $T_{\rm eff} = 3687 \pm 98$ K and $\log g = 4.80 \pm 0.03$). The 'photometric box' of GJ 588 was defined to assess if the physical parameters of GJ 588 are compatible with those of the models comprised in the 'asteroseismic box'. We used the $T_{\rm eff}$ and $\log g$ values given in the literature to define the box. In particular, we used $T_{\rm eff} = 3555 \pm 41$ K, and mass and radius determinations of 0.43±0.05 $M_\odot$ and 0.42±0.03 $R_\odot$ from Gaidos et al. (2014) to derive a $\log g = 4.82 \pm 0.08$ (see Table 1).[6]

Additionally, in Fig. 13 we show the 'photometric box' of GJ 699 defined by $T_{\rm eff} = 3237 \pm 60$ K (Gaidos et al. 2014) and $\log g = 5.040 \pm 0.005$ derived from 0.15 ± 0.02 $M_\odot$ and 0.187 ± 0.001 $R_\odot$ (Boyajian et al. 2012), along with the black stars pointing the models that excite periods at ∼10.83 d^{-1} and diamonds for periods at 23.12 d^{-1}. We also show the evolutionary tracks that cross the photometric or the asteroseismic boxes of GJ 588 and GJ 699. For the sake of clarity, we only show the evolutionary tracks that have similar metallicity and mass as the stars under study.

[6] Neves et al. (2013) and Bonfils et al. (2013) give $T_{\rm eff} = 3325 \pm 80$ K for GJ 588. However, from the evolutionary tracks in Baraffe et al. (1998) and RL14 this value is in clear contradiction with the mass given by the same authors: thus, if $M = 0.47\,M_\odot$ holds, then $T_{\rm eff} > 3400$ K; otherwise the mass would correspond to ∼0.2 $M_\odot$ models.

In the case of GJ 588, the 'photometric box' resulted to be traversed by 12 tracks with masses between 0.15 and 0.50 $M_{\odot}$; while the 'asteroseismic box' was traversed by 19 tracks with masses in the 0.20–0.50 $M_{\odot}$ range. Consequently, evolutionary tracks within the boxes encompass the 0.43 $M_{\odot}$ mass determination from the literature. The excited models within the GJ 588 asteroseismic box have masses in the 0.45–0.50 $M_{\odot}$ range corresponding to low-radial, low-degree $\ell = 1$ and $\ell = 2$, g modes. In particular, the excited model in the overlapping boxes has 0.45 $M_{\odot}$, which would give theoretical support to the putative signal.

On the contrary, results for GJ 699 point to a very different situation. In this case, even when the tracks falling within the 'photometric box' are in good agreement with the mass determination in the literature (six tracks with 0.10–0.20 $M_{\odot}$). The excited models at ∼23.12 d^{-1} (∼63 min) and ∼10.38 d^{-1} (∼2.3 h), indicated in Fig. 13 with stars and diamonds, respectively, correspond to masses (0.40–0.60 M⊙) that do not comprise GJ 699 lower mass determination from the literature. Therefore, our pulsation analysis does not support the presence of oscillations in GJ 699, which we recall was out (but close to the edge) of the instability region.

4.3 Completeness and signal detectability limit in the sample

In this section, we set up an upper limit for the intranight precision of the HARPS spectrograph. Therefore, if stellar pulsations on M dwarf stars exist and induce Doppler shifts in the spectra, such upper limit would indicate the amplitude threshold that we would be able to detect with a CTB-like campaign in either the RVs or any other index.

We performed the following experiment using GJ 588 as reference. We preferred GJ 588 over GJ 699 because, even when they are equally stable, GJ 588 has more data points, and a simpler window function. First, we randomized the RV measurements to create the time series of the noise with the observed time span. Later, we added simulated sinusoids of increasing amplitudes (from 0.2 up to 0.8 m s^{-1} in steps of 0.02 m s^{-1}) and random phases. Besides, we tested different frequencies ranging from 0 to 70 d^{-1} to sample the pulsation frequency domain and to measure the dependence of the threshold with frequency. Secondly, we calculated likelihood periodograms and we checked when our method succeeded in recovering the amplitude and frequency injected ('positive experiment'). In particular, we performed one hundred experiments for each input amplitude and frequency, varying the noise in all cases. The criterion we chose to define an experiment as positive was to recover both an amplitude within ±40 per cent of the input value and a frequency within the resolution range given by the inverse of T, the total time span of the observing run. Such criteria account for the typical large uncertainties of the amplitudes close to the detection limit and ensures the rejection of the experiments with large FAPs.

Finally, we defined the completeness at a certain frequency as the percentage of positive experiments recovered at each input amplitude; thus, the completeness increases with increasing amplitude, as expected. Consequently, fitting a simple S-shape function (or sigmoid function) we could define the limiting amplitude required to reach a 90 per cent completeness with HARPS (see Fig. 14).

Results for different input frequencies within the stellar pulsation range shown in Fig. 15 indicate that, in spite of the frequency dependence, if stellar pulsations exist and induce Doppler signals, we will not be able to detect them with HARPS if the induced signal has an amplitude below 0.5 m s^{-1}. The putative signal found in the GJ 588 RVs at 12.04 d^{-1} (red solid vertical line in Fig. 10),

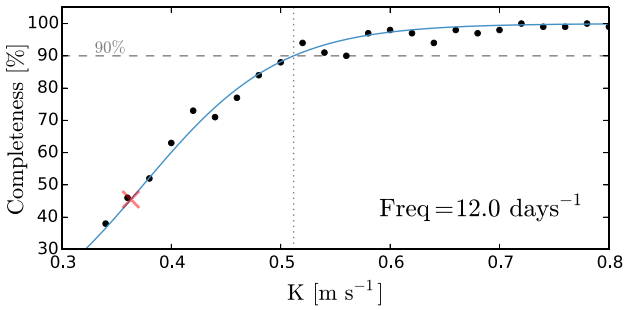

Figure 14. Completeness assessment of a 12 d^{-1} putative signal. The black dots indicate the proportion of experiments (completeness, y-axis) for which our analysis tools can recover the true amplitude (K, x-axis) injected at the different simulated input sinusoids. The blue solid line is an S-shape function fitted to the black dots. The horizontal grey dashed line indicates the 90 per cent completeness level. A periodic physical phenomenon with a frequency of 12.0 d^{-1} should produce a Doppler signal with a minimum amplitude of 0.51 m s^{-1} (vertical grey dotted line) to be easily detected with HARPS with a 90 per cent probability. The red cross (0.36 m s^{-1}) indicates the amplitude of the putative signal detected on GJ 588. It corresponds to a low 45 per cent completeness.

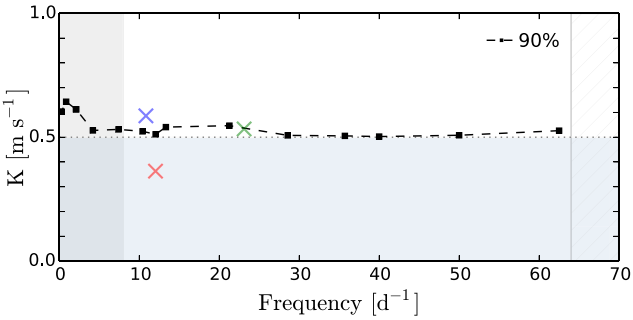

Figure 15. Limiting amplitudes detectable with a 90 per cent completeness as a function of the frequency (black dashed line). The grey left area is out of the pulsation range. The stripped right area indicates frequencies non-accessible for being of the order of the exposure time of the observations. The blue area highlights the general range of inaccessible signals, i.e. those with amplitudes below 0.5 m s^{-1}. The GJ 588 putative signal (red cross) is below the amplitude detection limit. The GJ 699 putative signals (blue and green crosses) are above the limit but the poorer sampling of the GJ 699 observations degrades the completeness 90 per cent limit up to ∼1.20 m s^{-1} seriously diminishing our sensitivity.

for which we measure an amplitude of 0.36 m s^{-1}, lies in a region where the completeness is only ∼45 per cent, which is consistent with recovering tentative, but inconclusive statistical evidence for such a signal (see red crosses in Figs 14 and 15).

The same experiment performed over the GJ 699 time baseline resulted in a more conservative detection limit (∼1.20 m s^{-1}). That crucial impact on the detectability of the signal is the result of having three nights of high-cadence data instead of four, and of having consecutive or non-consecutive observing nights that tangle the window function. In other words, even when both GJ 588 and GJ 699 are comparable in terms of stability, the more complicated window function of GJ 699 as a result of the sampling cadence might have prevented us from reaching higher sensitivity.

5 DISCUSSION AND CONCLUSIONS

Theoretical studies predict that main-sequence M dwarfs can oscillate with periods ranging from 20 min up to 3 h. The detection of such pulsations will open the whole field of asteroseismology for this spectral type; but first stellar pulsation on M dwarfs has to be observationally confirmed. This is one of the goals of the CTB, which makes use of the high-precision spectroscopy given by HARPS and HARPS-N to explore the short-time domain of a sample of M dwarfs with high-cadence observations.

The CTB thorough monitoring of the night using high-cadence observations deepens into a time domain that has not yet been widely explored by HARPS. As a result, we had to deal with some unexpected and not very well-known instrumental effects. In this study, we detailed the main corrections to be applied to deal with such effects and thus we set up a procedure for the analysis of the CTB data or in general, for the analysis of high-cadence, high-precision Doppler time series. We presented here the first results of the survey in search for stellar pulsations in M dwarfs. In particular, we focused on GJ 588 and GJ 699 (Barnard's star), two of the most long-term stable star targets of the sample (i.e. with no planet or strong activity reported so far) for which CTB collected four and three whole data nights, respectively.

Even when no signals compatible with pulsations were detected above the classical confidence thresholds (FAP = 1 per cent in the case of the likelihood periodograms, or 4σ in the case of the power spectra), we detected some excess of power in the periodograms and their power spectra for the two targets. More and higher precision data would be needed to confirm or refute them.

Giving serious thought to the fact that the signals could be caused by stellar oscillations, we have checked their compatibility with pulsation models. Results indicate that the putative signal at 12 d^{-1} ($\sim$2 h) found for GJ 588 would be compatible with low-radial, low-degree $\ell = 1$ and $\ell = 2$ g modes produced in stellar theoretical models also compatible with GJ 588 physical parameters in terms of mass, age, $T_{\rm eff}$ and $\log g$. On the contrary, GJ 699 was found not to be simultaneously compatible with any excited model in terms of its physical parameters and the periods of its putative signals.

Finally, we derived an amplitude detection limit for the detection of pulsations in M dwarfs with HARPS. Results indicated that no signal below $\sim$0.5 m s^{-1} can be detected with a confidence level better than 90 per cent on the most Doppler stable M dwarf studied so far (GJ 588). To obtain this limit, we used the standard CTB observational strategy for the pulsations science case. The higher threshold derived for GJ 699 – for which we only get three non-consecutive nights – demonstrates the crucial impact of the observational cadence in the detectability of a pulsation signature. The success of any spectroscopic program searching for pulsations will ultimately rely on even higher precision, but also on optimal sampling strategies.

Before solar-like oscillations were finally detected, many studies on different spectral type stars reported hints of power excess. This was the case of the G2V star α Cen A, for which several studies (e.g. Schou & Buzasi 2001) reported an excess of power before solar-like oscillations were finally confirmed by Bouchy & Carrier (2001, 2002) using the spectrometer CORALIE. This final confirmation came hand in hand with the rapid improvement of spectrographs, which aimed at detecting the first exoplanets. This could also end up being the case for M dwarfs pulsations. If the theoretical studies are accurate and the driving mechanisms can efficiently develop oscillations in M dwarf stars either: (i) the amplitudes are very low thus its confirmation requires of more precise spectrographs [e.g. the forthcoming Echelle Spectrograph for Rocky Exoplanet and Stable Spectroscopic Observations (ESPRESSO)/Very Large Telescope (VLT); Pepe et al. 2010, or High Resolution Spectrograph (HIRES)/European Extremely Large Telescope (E-ELT); Zerbi et al. 2014 or (ii) the size of the sample combined with a possible non-pure instability region is preventing us from having an observational confirmation (e.g. only $\sim$40 per cent of the δ Scuti within its instability region present oscillations; Balona & Dziembowski 2011).

In spite of this result, the 'CTB' survey takes us one step closer to the observational detection of M dwarfs pulsations and illustrates the challenges of high precision experiments, even with current state-of-the-art instrument like HARPS. Besides enlarging our observed sample with HARPS and HARPS-N, we plan to extend the search to ESPRESSO in the near future to monitor the two islands of instability predicted by RL14. Our aim is to build up a more targeted asteroseismology sample where models predict pulsations to be more conspicuous.

ACKNOWLEDGEMENTS

We acknowledge funding from AYA2014-30147-C03-01 by MINECO/Spain. This study is based on observations made with the 3.6-m ESO Telescope at la Silla under programme ID 191.C-0505. We acknowledge Stefan Dreizler, Enrico Gerlach, Sandra Jeffers, James Jenkins, Christofer Marvin, Julien Morin, Aviv Ofir, Ansgar Reiners and Ulf Seemann for their participation in the preparation of this programme proposal and their support and useful discussions. The authors thank the referee T. Böhm for his suggestions that helped improved this paper.

REFERENCES

Anglada-Escudé G., Butler R. P., 2012, ApJS, 200, 15
Anglada-Escudé G., Tuomi M., 2015, Science, 347, 1080
Anglada-Escudé G. et al., 2016a, Nature, 536, 437
Anglada-Escudé G. et al., 2016b, ApJ, 830, 74
Balona L. A., Dziembowski W. A., 2011, MNRAS, 417, 591
Baluev R. V., 2009, MNRAS, 393, 969
Baraffe I., Chabrier G., Allard F., Hauschildt P. H., 1998, A&A, 337, 403
Barnes J. R., Collier Cameron A., Unruh Y. C., Donati J. F., Hussain G. A. J., 1998, MNRAS, 299, 904
Barnes J. R. et al., 2012, MNRAS, 424, 591
Bedding T. R. et al., 2007, ApJ, 663, 1315
Berdiñas Z. M., Amado P. J., Anglada-Escudé G., Rodríguez-López C., Barnes J., 2016, MNRAS, 459, 3551
Boisse I., Bouchy F., Chazelas B., Perruchot S., Pepe F., Lovis C., Hébrard G., 2010a, European Phys. J. Web Conf., 16, 02003
Boisse I. et al., 2010b, A&A, 523, A88
Bonfils X. et al., 2013, A&A, 549, A109
Bouchy F., Carrier F., 2001, A&A, 374, L5
Bouchy F., Carrier F., 2002, A&A, 390, 205
Bouchy F., Bazot M., Santos N. C., Vauclair S., Sosnowska D., 2005, A&A, 440, 609
Bouchy F., Isambert J., Lovis C., Boisse I., Figueira P., Hébrard G., Pepe F., 2009, EAS Publ. Ser., 37, 247
Bouchy F., Díaz R. F., Hébrard G., Arnold L., Boisse I., Delfosse X., Perruchot S., Santerne A., 2013, A&A, 549, A49
Bourrier V., Hébrard G., 2014, A&A, 569, A65
Boyajian T. S. et al., 2012, ApJ, 757, 112
Breger M. et al., 1993, A&A, 271, 482
Choi J., McCarthy C., Marcy G. W., Howard A. W., Fischer D. A., Johnson J. A., Isaacson H., Wright J. T., 2013, ApJ, 764, 131
Cumming A., 2004, MNRAS, 354, 1165

Dawson R. I. et al., 2014, ApJ, 791, 89
Donati J.-F., Semel M., Carter B. D., Rees D. E., Collier Cameron A., 1997, MNRAS, 291, 658
Dressing C. D., Charbonneau D., 2013, ApJ, 767, 95
Fogtmann-Schulz A., Hinrup B., Van Eylen V., Christensen-Dalsgaard J., Kjeldsen H., Silva Aguirre V., Tingley B., 2014, ApJ, 781, 67
Gaidos E. et al., 2014, MNRAS, 443, 2561
Gray D. F., Desikachary K., 1973, ApJ, 181, 523
Henry T. J., Jao W.-C., Subasavage J. P., Beaulieu T. D., Ianna P. A., Costa E., Méndez R. A., 2006, AJ, 132, 2360
Huber D. et al., 2013, Science, 342, 331
Koen C., Kilkenny D., van Wyk F., Marang F., 2010, MNRAS, 403, 1949
Krisciunas K., Griffin R. F., Guinan E. F., Luedeke K. D., McCook G. P., 1995, MNRAS, 273, 662
Lehmann H., Mkrtichian D. E., 2004, A&A, 413, 293
Lo Curto G. et al., 2012, Proc. SPIE, 8446, 84461W
Lomb N. R., 1976, Ap&SS, 39, 447
Lovis C., Fischer D., 2010, in Seager S., ed., Exoplanets. Univ. Arizona Press, Tucson, AZ, p. 27
Neves V., Bonfils X., Santos N. C., Delfosse X., Forveille T., Allard F., Udry S., 2013, A&A, 551, A36
Neves V., Bonfils X., Santos N. C., Delfosse X., Forveille T., Allard F., Udry S., 2014, A&A, 568, A121
Pepe F. A. et al., 2010, Proc. SPIE, 7735, 77350F
Pepe F. et al., 2011, A&A, 534, A58
Perruchot S. et al., 2008, Proc. SPIE, 7014, 70140J
Reegen P., 2007, A&A, 467, 1353
Reid I. N., Hawley S. L., Gizis J. E., 1995, AJ, 110, 1838
Reiners A., Joshi N., Goldman B., 2012, AJ, 143, 93
Rodríguez E., Rodríguez-López C., López-González M. J., Amado P. J., Ocando S., Berdiñas Z. M., 2016, MNRAS, 457, 1851
Rodríguez-López C., MacDonald J., Moya A., 2012, MNRAS, 419, L44
Rodríguez-López C., MacDonald J., Amado P. J., Moya A., Mullan D., 2014, MNRAS, 438, 2371 (RL14)
Santerne A. et al., 2012, A&A, 545, A76
Santos N. C. et al., 2013, A&A, 556, A150
Scargle J. D., 1982, ApJ, 263, 835
Schou J., Buzasi D. L., 2001, in Wilson A., Pallé P. L., eds, ESA Special Publication, Vol. 464, SOHO 10/GONG 2000 Workshop: Helio- and Asteroseismology at the Dawn of the Millennium. ESA, Noordwijk, p. 391
Steffen J. H., Farr W. M., 2013, ApJ, 774, L12
Suárez Mascareño A., Rebolo R., González Hernández J. I., Esposito M., 2015, MNRAS, 452, 2745
Uytterhoeven K. et al., 2008, A&A, 489, 1213
Zechmeister M., Kürster M., Endl M., 2009, A&A, 505, 859
Zerbi F. M. et al., 1997, MNRAS, 290, 401
Zerbi F. M. et al., 1999, MNRAS, 303, 275
Zerbi F. M. et al., 2014, Proc. SPIE, 9147, 914723
Zhao F., Curto G. L., Pasquini L., Zhao G., 2014, in Haghighipour N., ed., Proc. IAU Symp. Vol. 293, Formation, Detection, and Characterization of Extrasolar Habitable Planets. Cambridge Univ. Press, Cambridge, p. 407
Zima W. et al., 2006, A&A, 455, 235

SUPPORTING INFORMATION

Supplementary data are available at *MNRAS* online.

Table 2. GJ 588 and GJ 699 RV and FWHM data used in this study.

Please note: Oxford University Press is not responsible for the content or functionality of any supporting materials supplied by the authors. Any queries (other than missing material) should be directed to the corresponding author for the article.

APPENDIX: DETAILED FREQUENTIST ANALYSIS

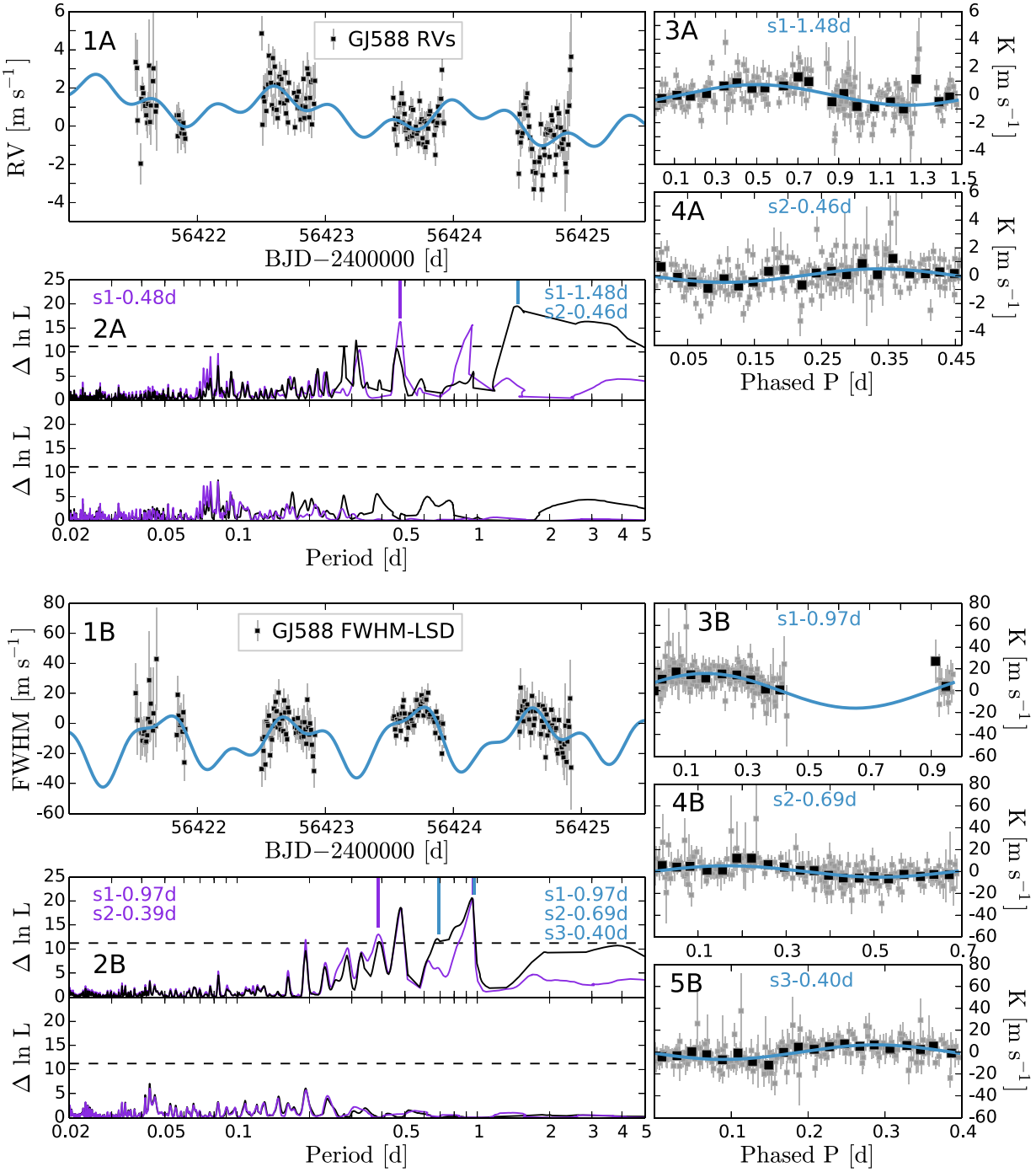

Figure A1. Periodic solutions for GJ 588 RVs (A panels) and FWHM-LSD (B panels) indices detected beyond the pulsational range ($P > 3$ h or $P > 0.125$ d). Instrumental distortions characteristic of the night (e.g. chromatic seeing or atmospheric dispersion among others) cause 1-d signals and submultiples. The light blue line plotted in panels 1A and 1B corresponds to the best model fitted to the observations (black squares) when we consider all the data as an single data set (see in panels 2A and 2B the corresponding periodograms in black). For the RVs, such model includes two sinusoids ($P_1 \sim 1.5$ d, and $P_2 \sim 0.5$ d), while for the FWHM-LSDs the model includes three sinusoids ($P_1 \sim 1$ d, $P_2 \sim 0.7$ d and $P_2 \sim 0.4$ d). Panels 3A, 4A and 3B, 4B and 5B show the data (grey squares) phased folded to each of these periodic signals (light blue lines). For the sake of clarity, bins of the observations are show with black squares. The periods of these signals are highlighted with light blue vertical lines in panels 2A and 2B. Purple periodograms in 2A and 2B panels result when we consider each night as an independent data set. This approach works as a filter for periods lower than 1 d. Regardless of the method used, we recover the same peaks in the range of study (20 min to 3 h), but we need simpler models with less sinusoids when we treat the nights independently (purple periodograms).

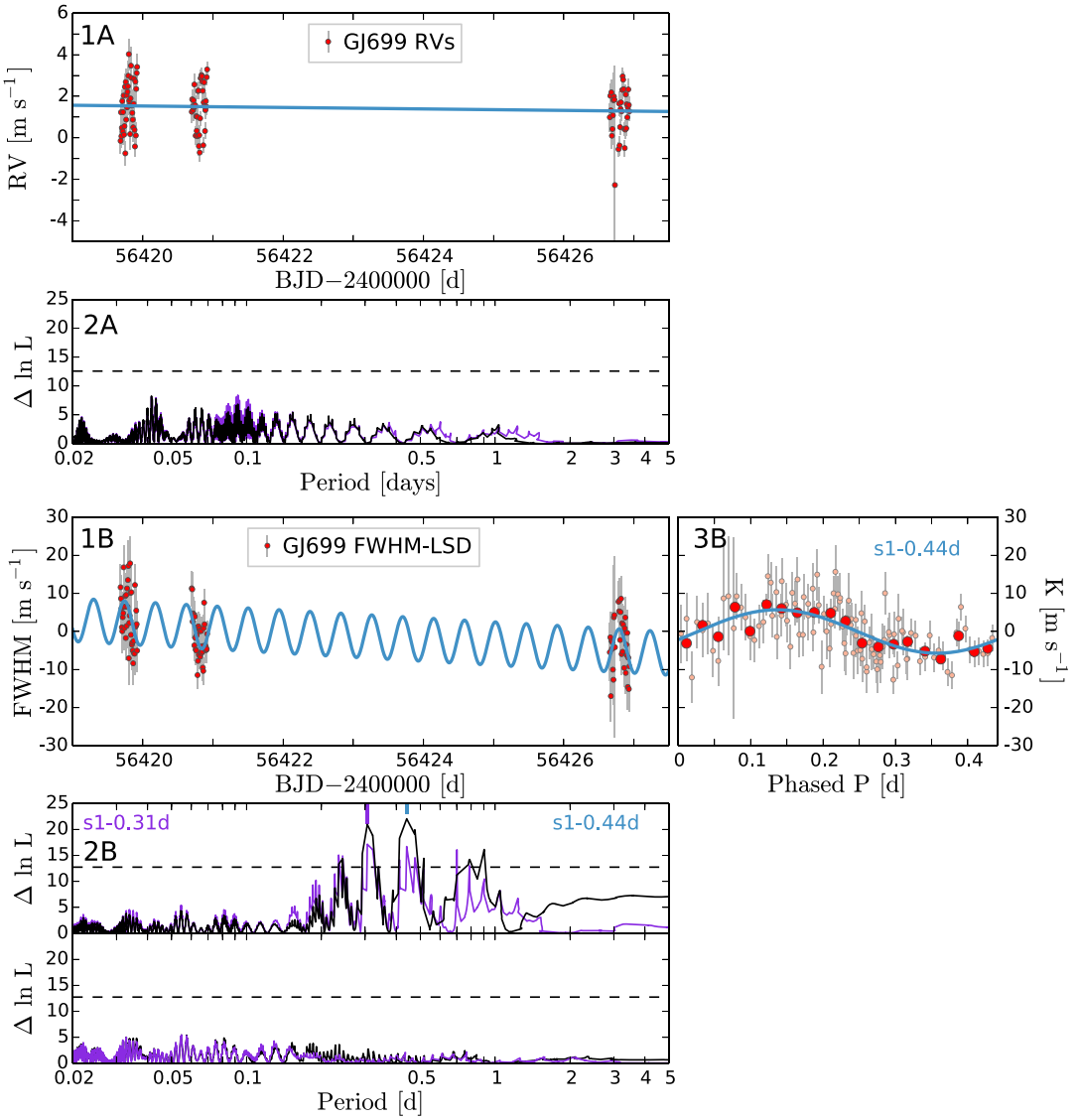

Figure A2. Periodic solutions for GJ 699 RVs (A panels) and FWHM-LSD (B panels) found in the $P > 3$ h (or $P > 0.125$ d) range. Panels 1A and 1B show the time series of the observations (red dots) and the best-fitting model (blue lines). Panels 2A and 2B show the likelihood periodograms. The black periodograms correspond to the analysis of the data as a single data set. The purple periodograms correspond to the analysis of the observations took at different nights as independent data sets. The blue lines in all panels correspond to models obtained in the case of a single data set analysis. Only one sinusoid had to be included for the FWHM-LSDs ($P \sim 0.4$ d in the case of a single data set analysis, and $P \sim 0.3$ d in the case of treating the nights independently). Panel 3B shows the observations phased folded to $P \sim 0.4$ d period. The big red dots are bins of the observations, which are indicated with smaller symbols.

This paper has been typeset from a TEX/LATEX file prepared by the author.